Simulating and quantifying multiple natural subsea CO_2 seeps at Panarea Island (Aeolian Islands, Italy) as a proxy for potential leakage from subseabed carbon storage sites

—

Supporting Information

Jonas Gros,[1,] Mark Schmidt,[1] Andrew W. Dale,[1] Peter Linke,[1] Lisa Vielstädte,[1] Nikolaus Bigalke,[1,2] Matthias Haeckel,[1] Klaus Wallmann,[1] and Stefan Sommer[1]*

[1] GEOMAR Helmholtz Centre for Ocean Research Kiel, RD2 / Marine Geosystems, Wischhofstr. 1-3, D-24148 Kiel, Germany

[2] present address: Geotek, 3 Faraday Close, Daventry, Northamptonshire, NN11 8RD, United Kingdom

* E-mail: jogros@geomar.de; telephone number: +49 431 600-2267.

This document provides: description of the bubble parametrization rack (section S-1); TAMOC example validation (section S-2); effect of CO_2 on seawater density (section S-3); composition of emitted gas at station PCTD3 and Bottaro Crater (section S-4); sensitivity of the Lagrangian advection-dispersion model to the time step (section S-5); validation of the Lagrangian advection-dispersion model (section S-6); initial bubble size distribution at station PCTD3 (section S-7); carbonate system model (section S-8); fluorescein release experiment (section S-9); simulation at vent C assuming non-circulating bubble interfaces (section S-10); validation of model simulation with individual pH measurements (section S-11); COMSOL Multiphysics simulation of water currents at station PCTD3 (section S-12); model predictions for low and high gas flow rates at station PCTD3 (section S-13); model predictions for 5–6 m above the seafloor at station PCTD3 (section S-14).

(23 pages)

S-1 Bubble parametrization rack

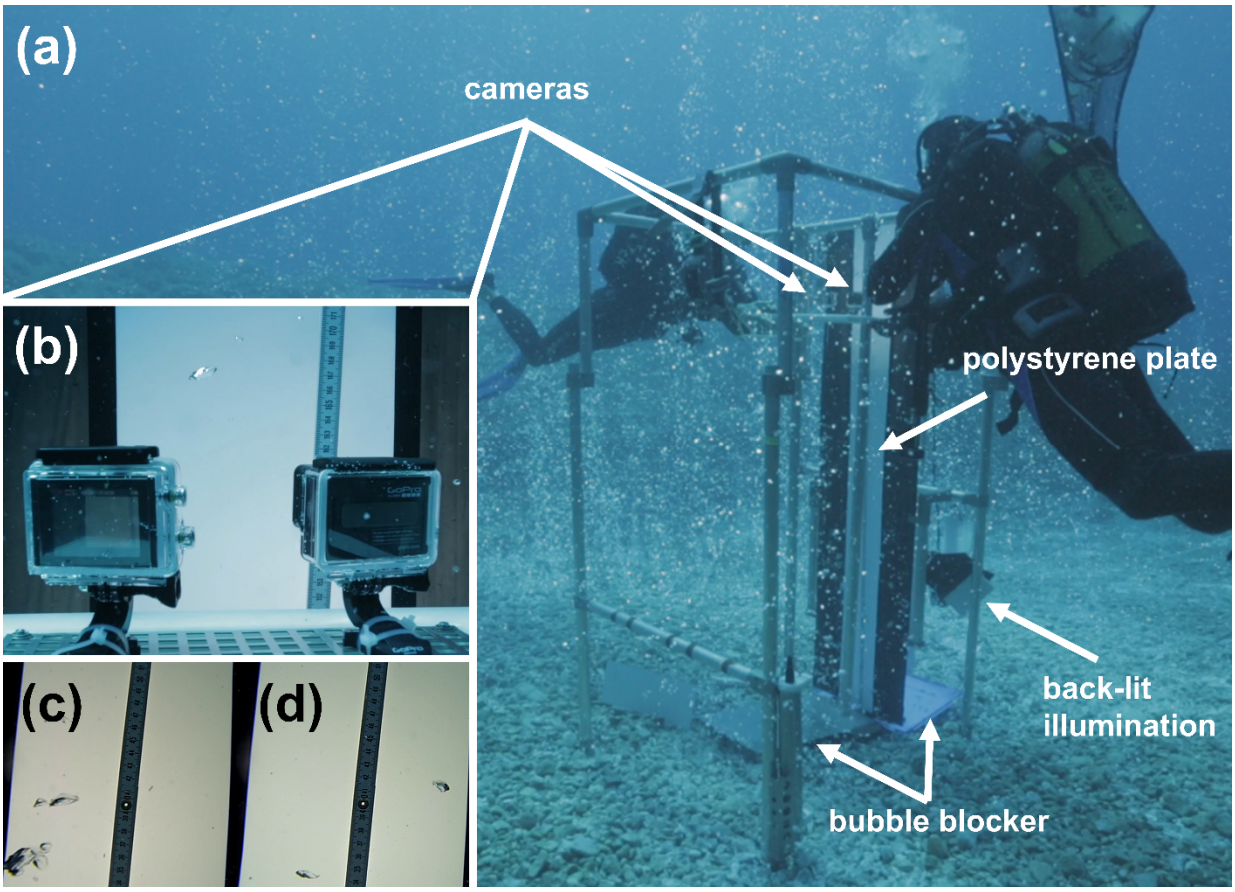

Figure S-1. (a) Bubble parametrization rack used to image the bubbles at Bottaro Crater. As described in the methods in the main text, tilted plates (bubble blocker) deployed at the seafloor permit only bubbles emitted at the vertical of the two cameras to enter the field of view. The polystyrene plate acts as a diffusor for the 17,000 lumen light source. (b) the two cameras (which can be moved up or down). (c–d) example frames of the recorded videos.

S-2 Validation of the TAMOC model with pre-existing literature data for carbon dioxide (CO_2)

Detailed validations of the Texas A&M oil spill (outfall) calculator (TAMOC) model have been presented previously, including the chemistry and bubble models, as well as single and multiphase plume models.[1–6] Here, a few example validations with literature data for carbon dioxide (CO_2) are presented for selected chemical properties. This section also compares the evolving diameter of a dissolving CO_2 bubble in the laboratory as reported by previous researchers with a simulation conducted with the TAMOC model, which is viewed as an aggregated validation of the several underlying estimates. Readers interested in further description and validation of the TAMOC model and of the underlying equations are referred to previous literature.[1–11]

The TAMOC model is tailored to a given compound solely by use of 10 chemical properties, which represent the sole compound-specific data that the user needs to supply. These chemical data are

supplied by default within TAMOC for 27 compounds, and data for >100 other individual hydrocarbon molecules have been compiled.[12] The chemical properties used for the present simulations are reported in Table S-1.[1,3]

Table S-1. Chemical properties used to tailor TAMOC simulations to the chemical compounds investigated.[1,3]

comp-ound	molecular weight, M (g mol^{-1})	critical pressure, P_c (MPa)	critical temperature, T_c (K)	critical volume, V_c (cm^3 mol^{-1})	molar volume of the solute at its normal boiling point, V_b (cm^3 mol^{-1})	acentric factor, ω (-)	Henry's law constant at 25°C and 101325 Pa, K_{H^*} (mol m^{-3} atm^{-1})	enthalpy of phase transfer from gas to water, $\Delta H_{gas\rightarrow H_2O}$ (kJ mol^{-1})	partial molar volume at infinite dilution in water, $\bar{v}^L$ (cm^3 mol^{-1})	Setschenow constant, K_{salt} (L mol^{-1})
CO_2	44.010	7.374	304.12	94.1	37.3	0.225	33.94	-19.7	32.0	0.132
H_2S	34.082	8.963	373.40	98.1	35.2	0.0948	101[a]	-17.9	34.9[a]	0.0462[a]
CH_4	16.043	4.599	190.56	98.6	37.7	0.011	1.43	-13.1	34.7	0.127
N_2	28.013	3.400	126.20	90.1	34.7	0.0372	0.63	-10.8	33.0	0.183
O_2	31.999	5.043	154.58	73.4	27.9	0.0216	1.3	-13.7	32.0	0.169
Ar	39.948	4.870	150.82	74.6	29.2	-0.004	1.4	-10.8	32.6[a]	0.169

[a] These values were updated relative to data available within version 1.1.1 of TAMOC. This includes the correction of an incorrect value of K_{H^*} for H_2S,[3] addition of the K_{salt} value for H_2S,[3,13] and addition of the $\bar{v}^L$ values for Ar and H_2S.[3,14]

Figure S-2 compares laboratory measurements and TAMOC predictions for CO_2 aqueous solubility at 298 K and varied pressures, showing good agreement with these data encompassing pressures equivalent to approximately 100–4,000 m water depth (where CO_2 is gaseous at the lowest pressures and liquid at the highest pressures). Another important parameter driving the rate of aqueous dissolution is the molecular diffusion coefficient in water. The molecular diffusion coefficient of CO_2 in pure water at 25°C is predicted to be $1.80 \cdot 10^{-9}$ m^2 s^{-1} by the Hayduk-Laudie formula[15] implemented in TAMOC, whereas values reported in the literature are $1.92 \pm 0.08 \cdot 10^{-9}$ m^2 s^{-1}.[16] The estimate in TAMOC is assumed representative of the diffusion of CO_2 over the water-side boundary layer surrounding gas bubbles. The small difference in molecular diffusion coefficients between the carbonate ions (CO_2, HCO_3^-, CO_2^{2-}) in water[17] is deemed negligible for environmental modeling in shallow seawater, where turbulent dispersion largely dominates over molecular diffusion for aqueously-dissolved CO_2 away from bubbles. Further example validation is presented below with a TAMOC simulation for literature data corresponding to a well-constrained laboratory experiment, viewed as an aggregated validation of the diverse components of the TAMOC model.

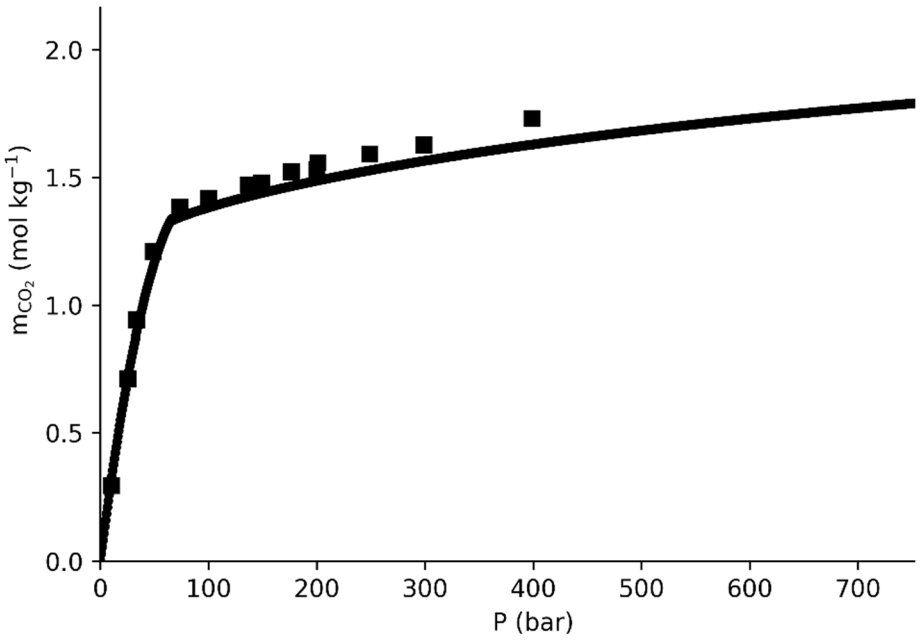

Figure S-2. Measured aqueous solubility of CO_2 in water at 298 K (m_{CO_2}, in mol kg^{-1}) from four different studies selected by Duan et al. 2006[18] (filled squares), overlaid with TAMOC predictions (solid line).

TAMOC can predict the behaviors of both "clean" and "dirty" CO_2 bubbles (Figure S-3), i.e. bubbles having either a circulating or a non-circulating interface.[7,19,20] Previously-reported field observations in both shallow and deep waters[21–23] indicate that circulating interfaces are necessary to explain field observations for pure CH_4 (above the hydrate stability zone), pure (gaseous) CO_2, predominantly-CO_2 natural gas (at Panarea), and pure Ar bubbles. In the laboratory, both circulating and non-circulating interfaces have been frequently observed (e.g. Figure S-3) and achievement of circulating interfaces in the laboratory often requires particular attention and use of ultra-clean water. However, except from the sea-surface micro-layer, seawater may often contain less surface-active solutes than tap water based on the observed effect on the air-water mass transfer rate,[24] which possibly explains why circulating interfaces are observed at sea. Recent laboratory data acquired with small (<1 mm diameter) bubbles in seawater (from 80 m depth) indicated non-circulating interfaces.[25] This apparent discrepancy in behavior with field observations conducted at sea with bubbles having diameters >1 mm[21–23] might be a consequence of low-level contamination, which would result in small bubbles having a non-circulating interface whereas large bubbles would present a circulating interface.[25] Subsea seeps of gases are usually reported to release most of their mass in the form of bubbles having >1 mm initial diameters.[26–33] In view of the convergent observations in the field for bubbles having diameters >1 mm,[21–23] in this work, bubbles at Panarea are simulated as having circulating bubble interfaces, confirmed by field observations of gas bubble composition with depth (see main text).

Figure S-3 compares TAMOC's prediction of the behavior of a gaseous CO_2 bubble within degassed pure water to data acquired in a controlled laboratory setting, with a circulating interface observed to transition to a non-circulating interface. The simulation agrees closely with the laboratory data, for the whole experiment duration, during which >99.8% of the initial bubble mass was lost through aqueous dissolution (last available radius measurement). As explained in the main text, simulations reported in this article

assumed circulating interfaces in the sea offshore Panarea. These simulations involve no tuning and are parameterized solely based on compound chemical properties (Table S-1) and objective field parameters (e.g. initial bubble size distribution, profiles of temperature, salinity, and dissolved chemicals in the water column). Consequently, these simulations are purely predictive.

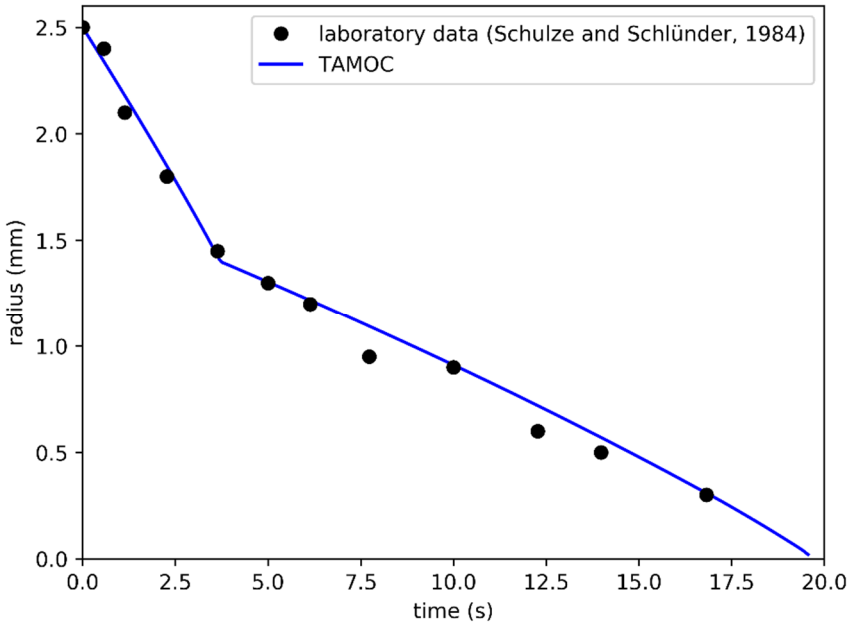

Figure S-3. Simulated (blue solid line) evolution of the radius of a CO_2 bubble compared to laboratory measurements within degassed deionized bidistilled water at 20±0.5°C.[34] Based on the observed mass transfer rates, the bubble was simulated as having a circulating interface for 3.7 s, and a non-circulating interface thereafter. Note that ~82% of the initial CO_2 aqueously dissolved before the transition in mass transfer rate was observed.

S-3 Effect of dissolved CO_2 on seawater density

Previous literature[35–39] computed usually the density of seawater containing dissolved CO_2 using a variant of equation S-1:

$$\rho(S,T,P,CO_2) = \rho(S,T,P) + C_{CO_2} - \rho(S,T,P) * \left(\frac{\bar{v}_{CO_2}}{M_{CO_2}}\right) * C_{CO_2} \quad \text{(S-1)}$$

where $\rho(S,T,P,CO_2)$ is the density of seawater containing added CO_2 (kg m^{-3}) at salinity *S*, temperature *T*, and pressure *P*, $\rho(S,T,P)$ is the density of seawater containing no added CO_2 (kg m^{-3}), C_{CO_2} is the concentration of the added CO_2 in the seawater (kg m^{-3}), $\bar{v}_{CO_2}$ is the partial molar volume of CO_2 at infinite dilution in water (m^3 mol^{-1}), and M_{CO_2} is the molecular weight of CO_2 (kg mol^{-1}).

Equation S-1 can be extended to consider additional dissolved species:

$$\rho(S,T,P,x) = \rho(S,T,P) + \sum_x(C_x) - \rho(S,T,P) * \sum_x\left(\left(\frac{\bar{v}_x}{M_x}\right) * C_x\right) \quad \text{(S-2)}$$

Where *x* are the dissolved species considered. Here, we consider the three species CO_2, HCO_3^-, and CO_3^{2-}. The concentrations of CO_2, HCO_3^-, and CO_3^{2-} are calculated as a function of the pH using the csys software[40] as described in the text. We assumed $\bar{v}_{CO_2}$ = 32.0 cm^3 mol^{-1} (Table S-1), $\bar{v}_{HCO_3^-}$ = 24.39 cm^3 mol^{-1}, and $\bar{v}_{CO_3^{2-}}$ = -4.07 cm^3 mol^{-1}.[41]

Based on assumed seawater properties for the Mediterranean Sea (main text), the calculated seawater density modification (relative to the background pH) induced by a range of observed pH levels are presented in Figure S-4. The magnitude of the density modification is relatively limited for the pH levels observed offshore Panarea. For example, an observed pH of 7.8 would lead to an increase of seawater density of ~0.0032 kg m^{-3} relative to pristine seawater, i.e. this water would be as dense as pristine water situated just 6.5 cm lower in the water column, based on a CTD profile acquired at station PCTD3 (estimate calculated at ~50 m water depth). The minimum pH measured in the field at station PCTD3 was 7.8. It appears consequently that the effect of dissolved CO_2 is minor at station PCTD3 and beyond the vertical positioning resolution achievable by the selected instrumentation for monitoring the dissolved CO_2 concentrations.

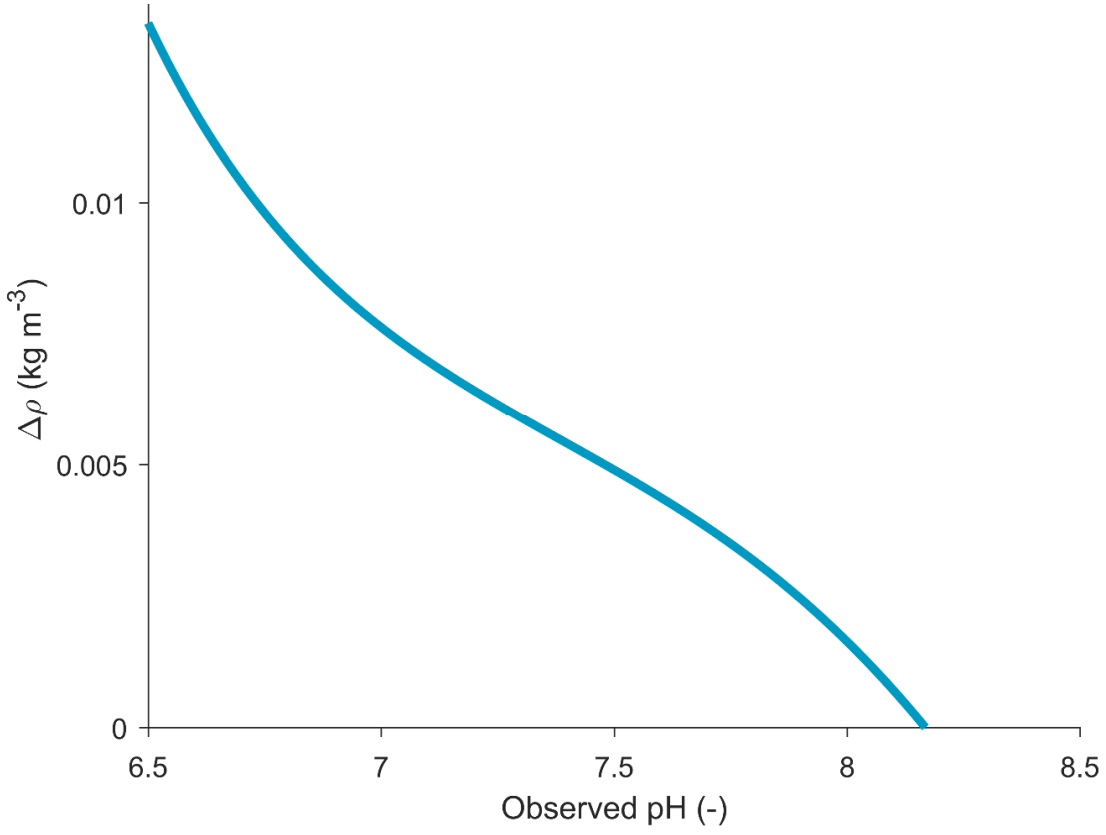

Figure S-4. Predicted difference in seawater density (Δρ) brought by dissolved CO_2 relative to seawater density at background pH, plotted as a function of the observed pH level. Values were calculated with equation S-2 assuming equilibrium in the carbonate system calculated with the csys software[40] using the properties of Mediterranean seawater listed in the main text (total alkalinity of 2.600 mmol kg^{-1} and background DIC of 2.269 mmol kg^{-1}), at conditions relevant for ~50 m water depth at Panarea in May 2014 (temperature of 15°C, absolute pressure of 6·10^5 Pa, and salinity of 37.85).*
** here and in the main text, we follow the convention of the UNESCO 1978 "Practical Salinity Scale" defining salinity as a unitless quantity,[42–44] which was previously reported as having units of g kg^{-1}.*

S-4 Assumed composition of gas emitted at Panarea for simulations

Table S-2. Average composition of bubbles sampled at the seafloor at two locations (43.5 and 44.4 m below the sea surface) at station PCTD3, using a stainless steel cylinder having a funnel-shaped inlet, operated by the ROV PHOCA.[45] And average composition at Bottaro Crater based on four bubble samples taken at the seafloor within the weaker seepage area on May 12 and 13 (two samples on each day, same sampling procedure as described in the main text for samples collected at vent C).

chemical species	volume fraction at station PCTD3 (mean ± half of data range)	volume fraction at Bottaro Crater (mean ± standard deviation)
CO_2	0.9705±0.005	0.9624±0.023
N_2	0.0070[a]±0.004	0.0106[a]±0.0032
O_2	0[a]	0[a]
Ar	0[a]	0[a]
CH_4	0.0065±0.0025	$1.4 \cdot 10^{-5} \pm 1.3 \cdot 10^{-6}$
H_2S	0.016[b]±0.001	0.0270[b]±0.022

[a] for simulation purposes, the measured 'N_2/O_2+Ar' was assumed to consist exclusively of N_2

[b] assumed equal to the remaining, unquantified volume fraction; value in good agreement with previous field measurements at Panarea[46,47]

S-5 Sensitivity analysis of the Lagrangian advection-dispersion model with respect to the time step for station PCTD3

The Lagrangian advection-dispersion model was run 20 times with time steps ranging 5 to 300 s, and the estimated total mass flow rate for station PCTD3 was calculated (following the method described in the main text). This analysis indicated that the model is little sensitive to the time step size as long as the time step is ≤50 s (Figure S-5). For time steps >50 s, the estimated total mass flow rate at station PCTD3 decreases with increasing time step size. This analysis confirmed that the time step of 10 s chosen for the study leads to results that are largely independent of the step size.

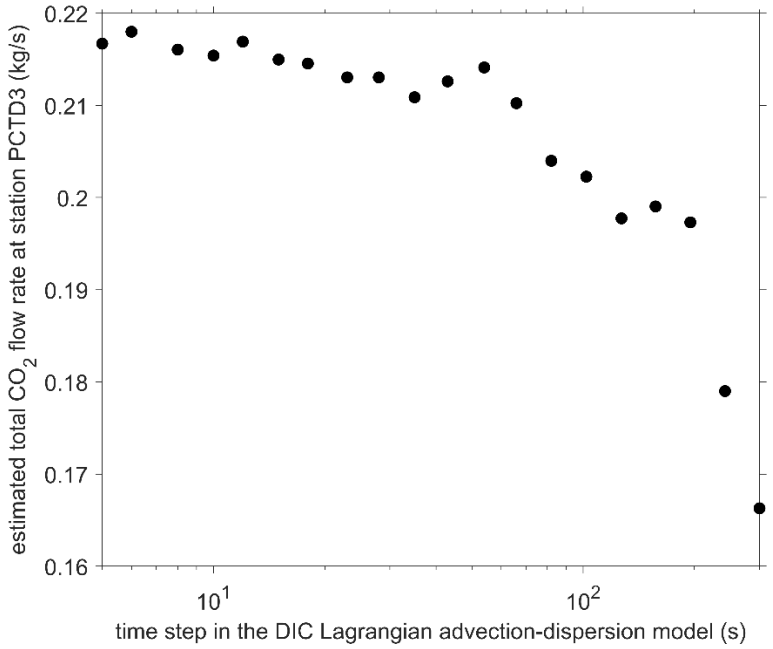

Figure S-5. Estimated total CO_2 flow rate predicted for station PCTD3 as a function of the time step in the Lagrangian advection-dispersion model. (Note that the TAMOC bubble model is run with an adaptive-step algorithm using a maximum step size of 0.1 s, for all cases.)

S-6 Validation of the implementation of the dissolved CO_2 Lagrangian advection-dispersion model with the analytical solution

Whereas both TAMOC and the csys model are existing softwares that have been validated in previous studies,[1–6,11,48–50] the Lagrangian advection-dispersion model is described here for the first time. While the model itself follows existing concepts,[e.g. 51] this section describes the validation of our particle-tracking algorithm implemented in Matlab. Consequently, predictions of the Lagrangian advection-dispersion model were compared with the analytical equation at steady state for a simple scenario implying a non-reactive chemical.

The advection-diffusion equation is:

$$\frac{\partial C}{\partial t} + u \cdot \frac{\partial C}{\partial x} + v \cdot \frac{\partial C}{\partial y} + w \cdot \frac{\partial C}{\partial z} = D_x \cdot \frac{\partial^2 C}{\partial x^2} + D_y \cdot \frac{\partial^2 C}{\partial y^2} + D_z \cdot \frac{\partial^2 C}{\partial z^2} \quad \text{(S-3)}$$

where x, y, z are positions in three dimensions; t is time; C is concentration; D_x, D_y, and D_z are the dispersion coefficients along the x, y, and z dimensions, respectively; and u, v, and w are the corresponding velocities.

For a simple continuous point source of a non-reacting chemical species emitted at the surface of a no-flux boundary at the seafloor and with water current aligned along the x dimension, the analytical solution at steady state is:[52]

$$C(x,y,z) = 2 \cdot \frac{\gamma \cdot \sqrt{\pi}}{\sqrt{\alpha}} \cdot e^{-2 \cdot \sqrt{\alpha \cdot \beta}} \quad \text{(S-4)}$$

with:

$$\alpha = \frac{(x-x_0)^2}{4 \cdot D_x} + \frac{(y-y_0)^2}{4 \cdot D_y} + \frac{(z-z_0)^2}{4 \cdot D_z} \quad \text{(S-5)}$$

$$\beta = \frac{U^2}{4 \cdot D_x} \quad \text{(S-6)}$$

$$\gamma = \frac{\dot{m}}{4\pi \cdot \sqrt{4\pi \cdot D_x \cdot D_y \cdot D_z}} \cdot e^{\frac{(x-x_0) \cdot U}{2 \cdot D_x}} \quad \text{(S-7)}$$

where $\{x_0, y_0, z_0\}$ is the location of the emission source; U is the water current along the x dimension; and $\dot{m}$ is the mass flow rate at the emission source.

The Lagrangian advection-dispersion model implementation was validated with the analytical solution given in eqs. S-4–S-7, assuming U = 0.1 m s^{-1}, $D_x = D_y = 10^{-2}$ m^2 s^{-1}, and $D_z = 10^{-3}$ m^2 s^{-1}. For this validation, a small time step (0.1 s) was used as well as a small grid size (small cubes of a 0.25 m side over a 50×50×5 m^3 volume). The analytical solution was numerically integrated over each grid cell for comparison with predictions of the Lagrangian model. The Lagrangian advection-dispersion model was run until steady state was achieved within the evaluation grid. When the number of parcels of the dissolved chemical is increased from ~$2 \cdot 10^5$ to ~$2 \cdot 10^7$, the predictions of the Lagrangian advection-dispersion model increasingly converge towards the analytical solution (Figure S-6a,b). Consequently, the model predicts correctly the processes in play as long as the time step is sufficiently small and the number of Lagrangian parcels is sufficiently large for the spatial resolution investigated.

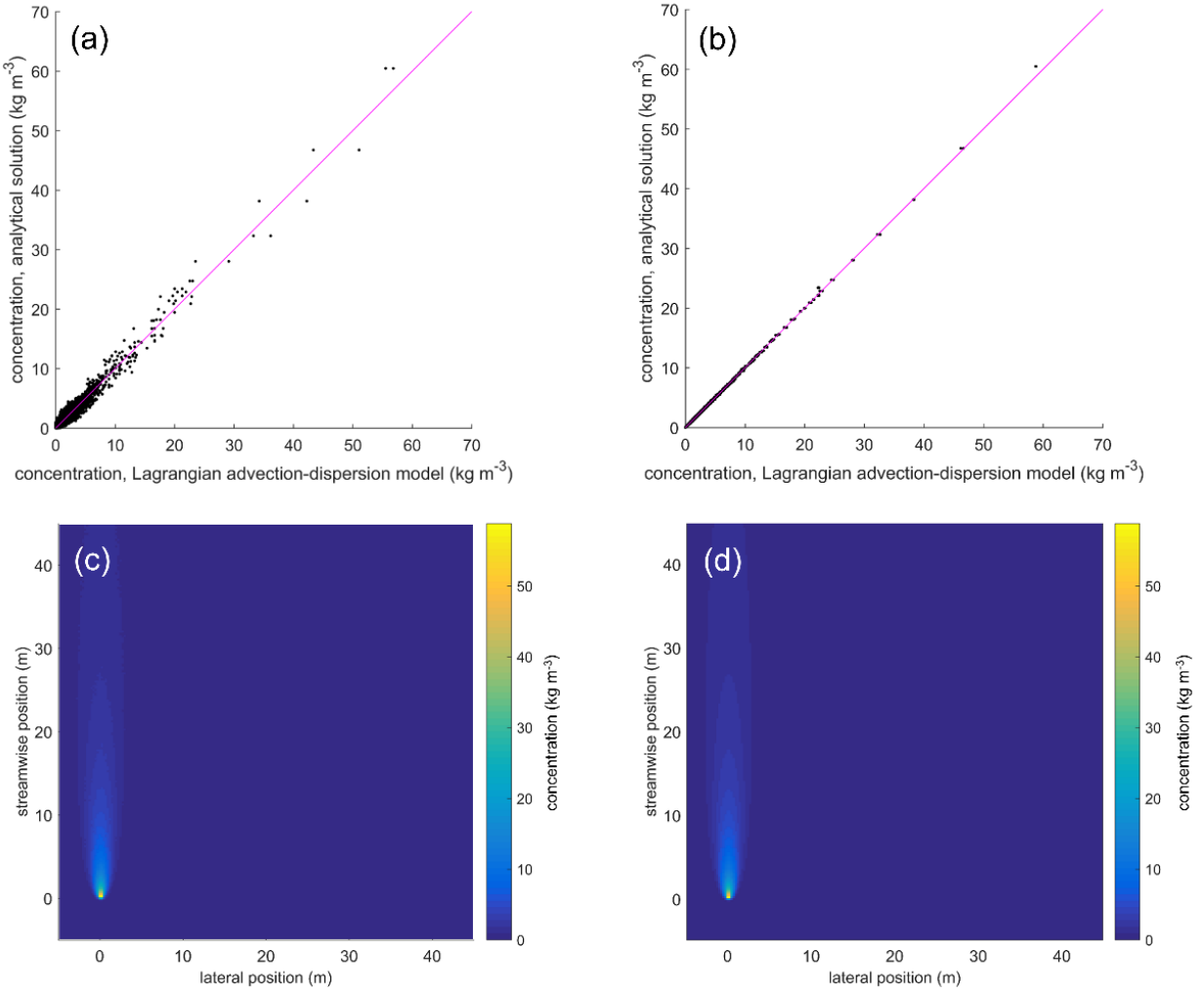

Figure S-6. Predicted concentrations for a non-reactive chemical species emitted from a point source situated on a reflective seafloor, at a mass flow rate of 1 kg s^{-1}. (a–b) comparison between the concentrations predicted with the analytical solution (eqs. S-4–S-7) and with the Lagrangian advection-dispersion model for a domain of 50×50×5 m^3 ($8 \cdot 10^5$ cells in total), using (a) ~$2 \cdot 10^5$ and (b) ~$2 \cdot 10^7$ parcels of dissolved chemical. The solid line has a unit slope and zero intercept. (c–d) predicted concentrations within the first 0.25 m above the seafloor according to (c) the Lagrangian advection-dispersion model using ~$2 \cdot 10^7$ parcels and (d) the analytical solution.

S-7 Initial bubble size distribution at station PCTD3

On May 9, 2014, bubbles exiting the seafloor at station PCTD3 were imaged with the GEOMAR bubble box.[53] The bubble box was positioned at three different seep sites, and the bubbles exiting the seafloor were imaged against a screen including a labeled scale. The measurement principle was similar to that of the bubble parametrization rack described in section S-1 and in the main text, and used at Bottaro crater. Consequently, we do not describe the bubble box further here, and refer to a previous publication for a more in-depth description of the instrument.[53] Here, the data of the bubble box were processed following the method described in main text for the determination of bubble size distributions at Bottaro crater. Observations at the three seep sites were combined, and 1072 bubbles were identified within 41 video

frames selected at a 2 min time interval (Figure S-7a). A measured volume flow rate of 0.33 L min^{-1} was used to scale the measurements. Bubbles at station PCTD3 had a volume median diameter (d_{50}) of 13.9 mm, with a bootstrap 95% confidence interval of 11.8–15.3 mm (Figure S-7a). This confidence interval was determined by 10,000 bootstrap resampling of the observed size distribution.[54] In order to decrease the computation burden, the size distribution was discretized with 6 bins (Figure S-7b), used in the TAMOC model for the simulations at station PCTD3. Simulation of the aqueous dissolution of gas bubbles confirmed that the 6 bins used to discretize the size distribution is sufficient to reproduce the gas bubble behavior (Figure S-7c), at an approximately 200-time lower computational cost.

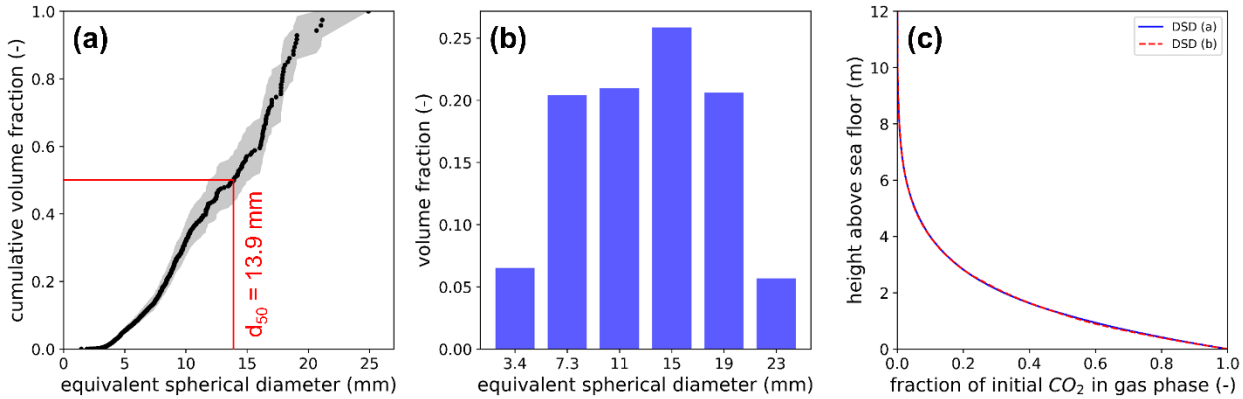

Figure S-7. (a) Observed initial bubble size distribution (DSD) at station PCTD3 on 9 May 2014 at 7:18–8:47 am (solid dots) and bootstrap 95% confidence interval (gray area). (d_{50} = volume median diameter). (b) Discretized bubble size distribution obtained by grouping the observed size distribution of panel (a) into six bins of equal size. (c) Fraction of the CO_2 released at a water depth of 51.22 m remaining within gas bubbles as a function of depth, according to two TAMOC simulations at station PCTD3 assuming either DSD (a), blue line, or DSD (b), red dashed line. The simulations reported on panel c indicate that initial bubble size distributions (a) and (b) lead to similar model predictions. Size distribution (b) was therefore used for simulations at station PCTD3.

S-8 Carbonate system model

In natural seawater, dissolved inorganic carbon (DIC) partitions into several different chemical species (CO_2, HCO_3^-, and CO_3^{2-}) through a series of chemical reactions that have been characterized in detail by previous researchers.[40] These reactions determine the non-linear equilibrium concentrations of the different chemical species and the resulting pH. The calculations depend primarily on the total alkalinity and (background + excess) DIC. Additional variables include the temperature, salinity, and pressure. However, these three last parameters varied within a narrow range at the (shallow) sites studied, and consequently the amount of DIC was the major driver to the simulated pH (alkalinity being assumed constant). Figures S-8 and S-9 provide two different visualizations of the carbonate system equilibrium as a function of the excess DIC.

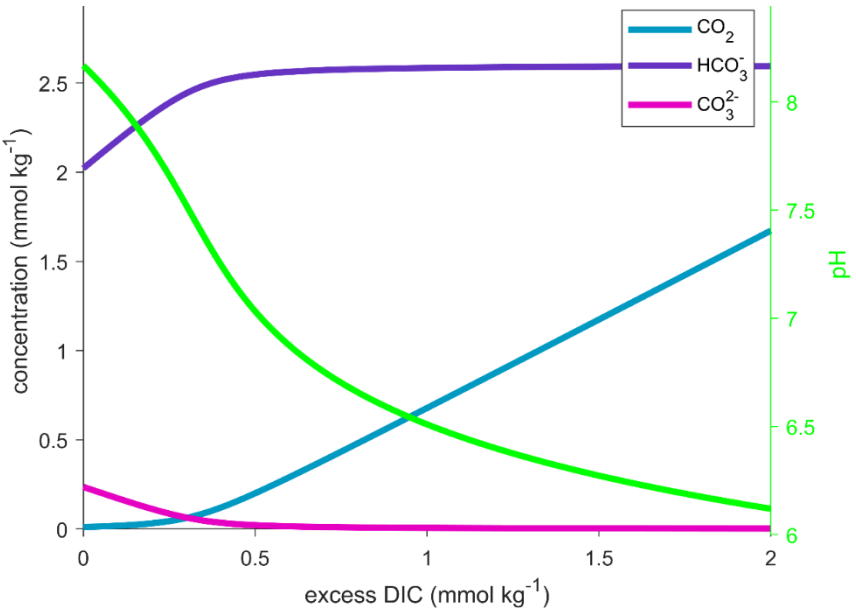

Figure S-8. Predicted equilibrium carbonate system (blue, purple, and pink lines, left axis) and pH (green, right axis) as a function of excess dissolved inorganic carbon (excess DIC) in seawater near Panarea Island. Values were calculated with the csys software[40] using the properties of Mediterranean seawater listed in the main text (total alkalinity of 2.600 mmol kg^{-1} and background DIC of 2.269 mmol kg^{-1}), at conditions relevant for ~50 m water depth at Panarea in May 2014 (temperature of 15°C, absolute pressure of 6·10^5 Pa, and salinity of 37.85).

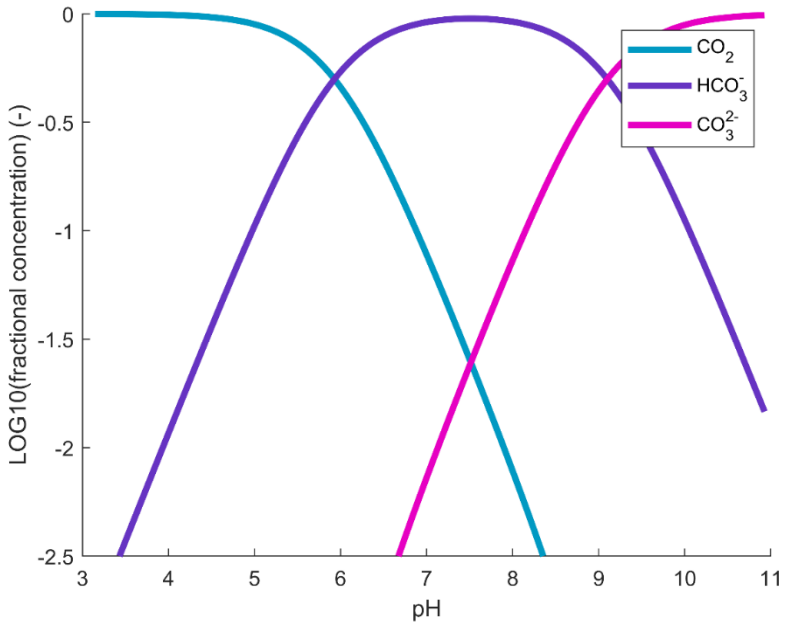

Figure S-9. Predicted equilibrium carbonate system as a function of pH in seawater near Panarea Island. Values were calculated with the csys software[40] using the properties of Mediterranean seawater listed in the main text (total alkalinity of 2.600 mmol kg^{-1}), at conditions relevant for ~50 m water depth at Panarea in May 2014 (temperature of 15°C, absolute pressure of 6·10^5 Pa, and salinity of 37.85). Fractional concentrations are defined as the ratio of the individual concentrations of each of the three chemical species to the sum of their three concentrations. Note: the effect of depth (pressure of 6·10^5 Pa to 1·10^5 Pa) was negligible at the studied sites (difference smaller than the width of the plotted lines). The effect of the up to 2°C temperature change within the water column at the studied site was larger than the effect of pressure, but still smaller than the width of the plotted lines. Consequently, the carbonate system was mostly driven by the excess DIC in our calculations.

The carbonate system model uses the csys software (https://www.soest.hawaii.edu/oceanography/faculty/zeebe_files/CO2_System_in_Seawater/csys.html), which represents the latest publicly-available update to the method described in detail by Zeebe and Wolf-Gladrow.[40] The model reported in this article uses the latest version available on 3rd October, 2018 (last updated on 7th April, 2014). Csys agrees closely with other softwares,[50,55–57] and it has been found that csys can be used interchangeably with a set of 9 other similar softwares for most purposes owing to the similarity in predictions among the 10 softwares.[50] Here are reported the equations used by the version of the csys software used in this work. This is done because there has been considerable confusion in the literature resulting from a significant number of typos in the publication of key coefficients,[50,58] because the current consensus that has arisen on most of the equations[50,56] may evolve, and because access to the csys code version used in this work may not be warranted in the future. (Unless otherwise noted, page numbers refer to the book of Zeebe and Wolf-Gladrow (2001),[40] third impression with corrections (2005).)

(a) Coefficients and equations in csys that follow exactly the book of Zeebe and Wolf-Gladrow (2001):[40]

The equilibrium constants follow recommended equations reported at pages 260 (bisulfate ion and hydrogen fluoride), 262 (boric acid), 264–265 (phosphoric acid), 266 (aragonite and calcite). Concentrations of sulfate, boron, and hydrogen fluoride are calculated from salinity.[40,59] The effect of pressure on the equilibrium constants follows the procedure defined at page 267, with coefficients from Table A.11.1 except for the differences described in (b). The equations are solved as described at pages 271–277 to derive the parameters of interest from the total alkalinity, background DIC, and any additional dissolved CO_2 input arising from simulated gas seepage. Within csys, the fugacity and Henry's law constant of CO_2 follow the method of Weiss (1974),[60] where the mole fraction of non-CO_2 gases in air (equation 9 of Weiss (1974)[60]) is assumed to be equal to 1.

(b) Coefficients or equations in csys that differ from the book of Zeebe and Wolf-Gladrow (2001):[40]

The ion product of water follows the recommended equation at page 258, with one coefficient (148.96502) corrected to 148.9652 on 4 March 2014 as described in a comment in the csys code. (The former coefficient was taken from a previous reference,[59] which itself cited another reference[61] using yet another value of this coefficient). The first and second acidity constants of the carbonic acid follow the refit of the Mehrbach et al. (1973)[62] data by Lueker et al. (2000)[63] as reported at page 255. (The book highlights different recommended equations than what is implemented as the default in the csys code; the recommended equations from the book are available in csys as an option, however the model used in the current article sticks to the default options in csys. The default Lueker et al. (2000)[63] refit of Mehrbach et al. (1973)[62] data is the recommended best practice[50,56]). Some errors in coefficient values from Table A.11.1 have been updated in the csys code with respect to the latest reprint of the book (2005). This concerns a sign correction for a_2 for K_B^* ($-2.608 \cdot 10^{-3}$), as described in the errata available on Richard Zeebe's web site (https://www.soest.hawaii.edu/oceanography/faculty/zeebe_files/CO2_System_in_Seawater/csys.html), and a correction of the K_W^* values from that in water reported in Table A.11.1 (a_0

= -25.60; a_1 = 0.2324; a_2 = $-3.6246 \cdot 10^{-3}$) to that in seawater (a_0 = -20.02; a_1 = 0.1119; a_2 = $-1.4090 \cdot 10^{-3}$).

(c) Change that we applied to the csys software of Zeebe and Wolf-Gladrow (2001):[40]

The csys code was edited to format it as a Matlab function, so that it can be easily called from other algorithms and exchange inputs and outputs; this was done purely for convenience and did not modify any of the algorithms used in csys.

S-9 Fluorescein injection experiment

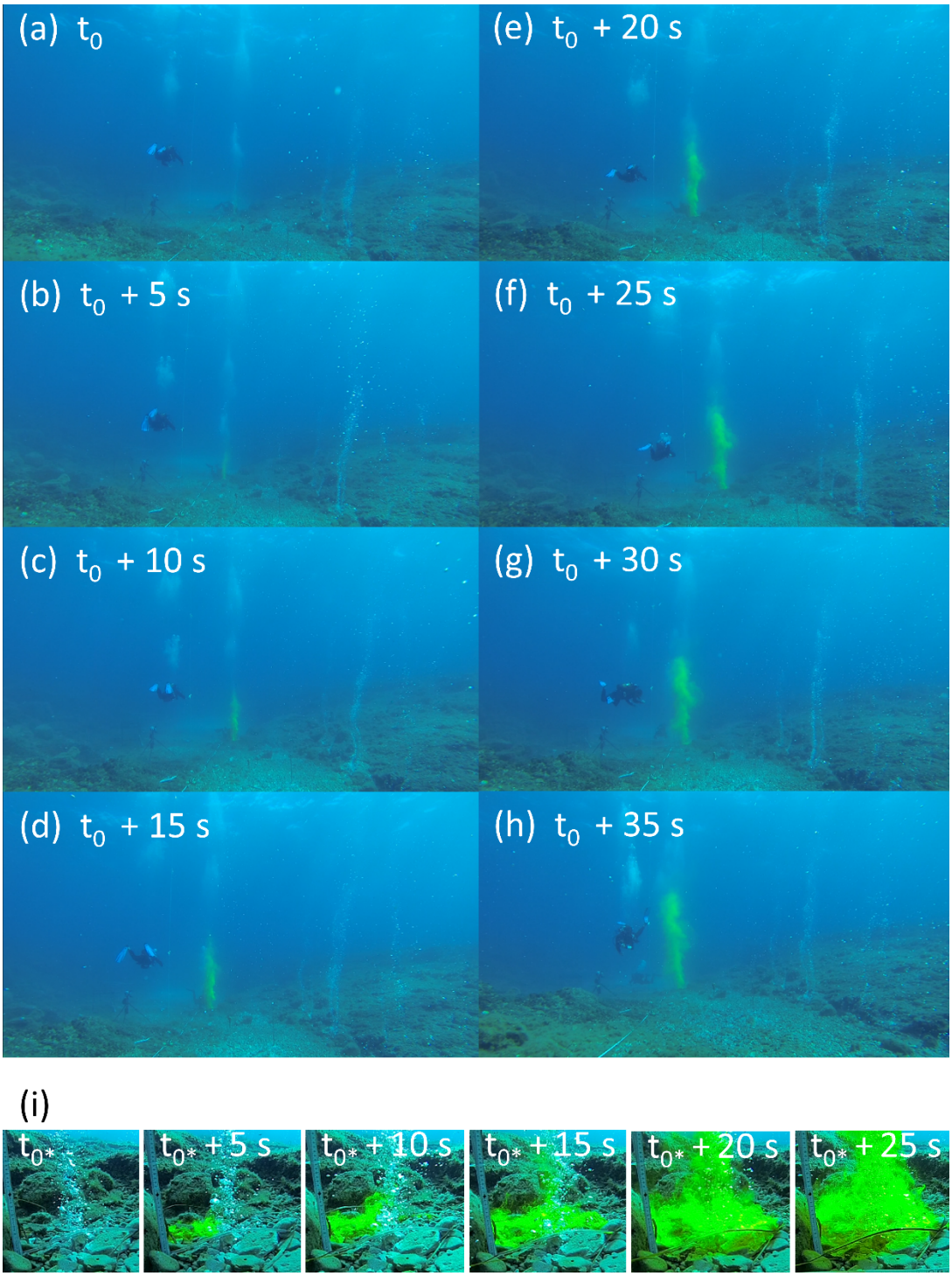

Figure S-10. Video snapshots throughout the fluorescein release experiment at vent C. (a–h) General view in a chronological sequence at a 5 s interval, (i) zoom on the release zone, showing the circular injection ring through which the dye was injected, at a 5 s interval. Image times are indicated relative to an arbitrary initial time point (t_0 for a–h and t_{0*} for i). The upwards movement of the dye indicates that a bubble plume formed, meaning that the ascending bubbles entrained ambient seawater upwards, transporting the dye. The scale visible in panel i is in centimeters.

S-10 Predicted average gas phase composition and fraction of CO_2 in the gas phase as a function of depth at vent C (Bottaro Crater) assuming non-circulating bubble interfaces

Field observations collected at vent C clearly indicate that bubbles behaved as bubbles having circulating interfaces (Figure 2b). On the contrary, the slower mass transfer rates resulting from assuming non-circulating interfaces would imply a strong mismatch with field observations (Figure S-11).

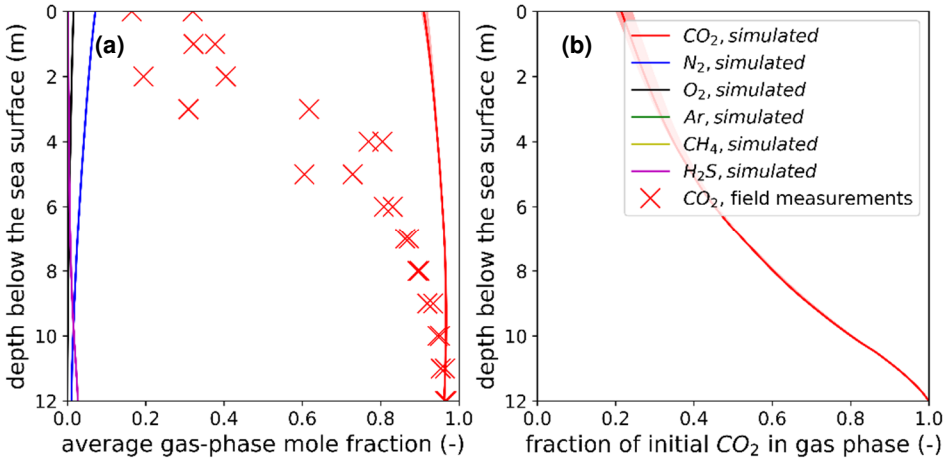

Figure S-11. (a) Evolving average composition of the gas phase from the emission source at 12 m depth (vent C) to the sea surface, as predicted by TAMOC when assuming non-circulating bubble interfaces for all simulated compounds (solid lines = measured size distribution, shaded area = 95% confidence interval as defined on Figure 2a), and measured in the field for CO_2 (crosses). (b) Fraction of the CO_2 released at the emission source remaining within gas bubbles as a function of depth, according to a TAMOC simulation assuming non-circulating interfaces.

S-11 Predicted versus measured pH at 1–2 m above seafloor for different total mass flow rates

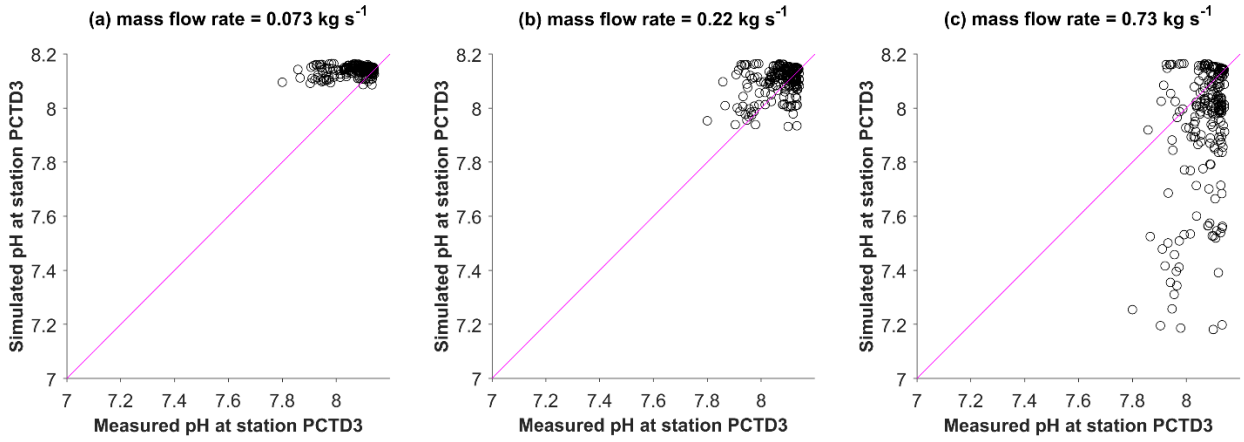

Figure S-12. Comparison between simulated pH and measured values at the 215 data points available at station PCTD3, for three different simulated total mass flow rates spanning an order of magnitude. The best estimate as defined in main text is plotted in (b). Measured pH are 1 min average values; the simulated values where calculated for the corresponding water volumes (10 m radius cylinder extending from 1–2 m above the seafloor).

S-12 Comsol Multiphysics simulation of water currents in the vicinity of station PCTD3

ADCP measurements were conducted approximately 200 m upstream from station PCTD3. In order to estimate the potential for local bathymetry to deflect water currents in-between these two points, a simplified simulation was conducted with the Comsol Multiphysics software (version 5.3). In this simulation, the local bathymetry was imported in Comsol Multiphysics and smoothed over a 10,000-nodes grid covering a region of approximately 900×2,500 m^2. A wall (no-slip) boundary was assumed on the Panarea Island side of the domain (west), whereas open (slip) boundaries were considered on the other sides (south and east). In this simulation, a southwards water current was applied at the North boundary of the domain (located at the latitude of the ADCP instrument). Predictions indicate that under these simplified assumptions water current was deflected by the raised seabed in the vicinity of Panarea Island, leading to a deflection by ~12° to the east for this scenario between the ADCP location and station PCTD3 (Figure S-13).

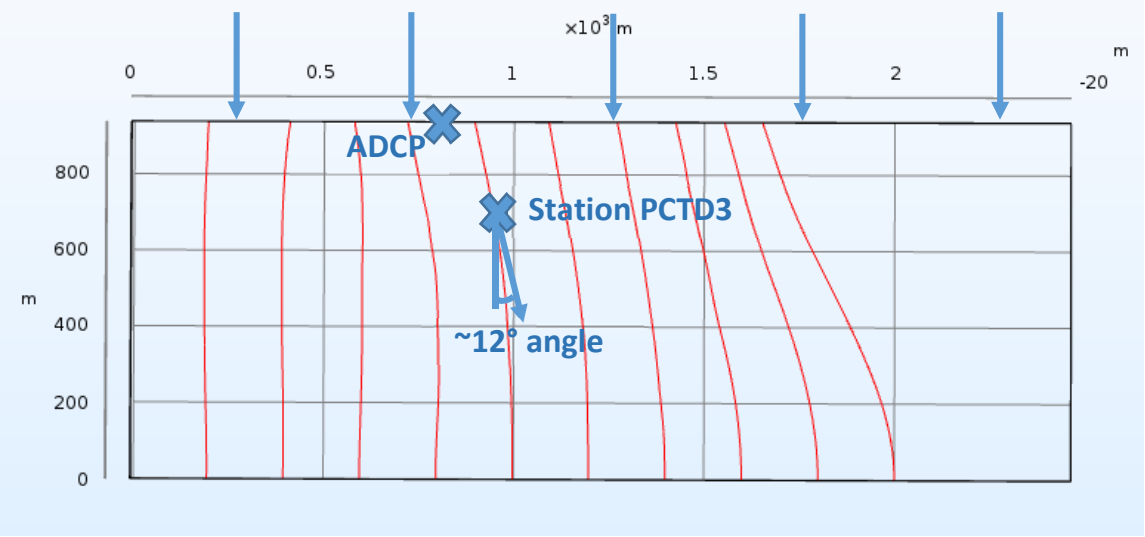

Figure S-13. Water current streamlines deflected by the local bathymetry as predicted with the Comsol Multiphysics software.

S-13 Predicted pH maps at 1–2 m above the seafloor assuming low and high total volume flow rates

Simulated pH maps for total mass flow rates one third (0.073 kg s^{-1}) and three times (0.73 kg s^{-1}) the best estimate of 0.22 kg s^{-1}.

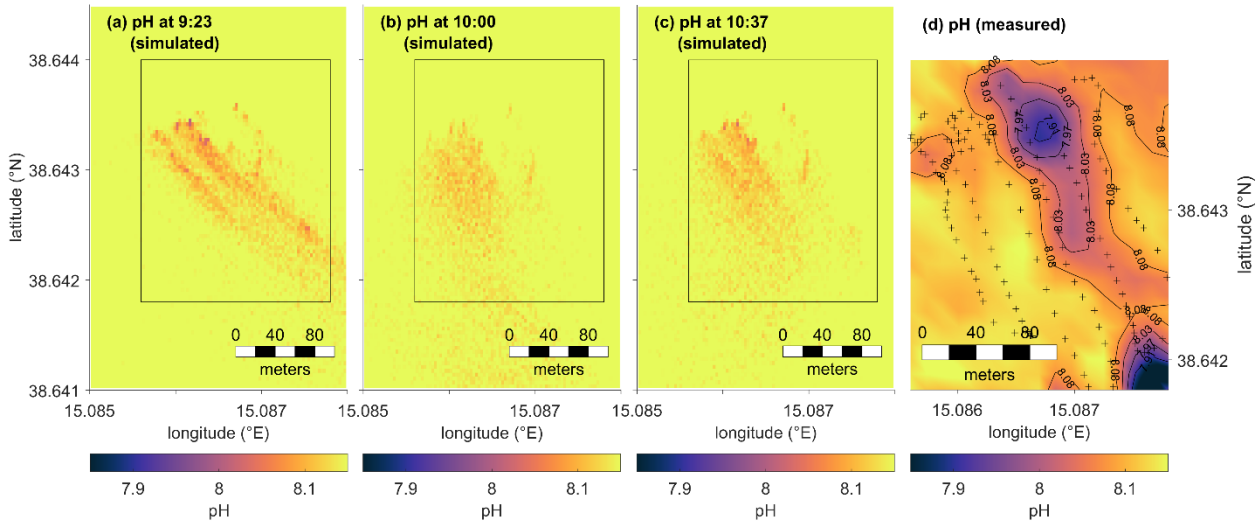

Figure S-14. (a–c) Simulated pH maps at three time points on 8 May 2014 for a total volume flow rate of 0.073 kg s^{-1} over the whole area (one third of the best estimate presented in Figure 3), and (d) observed map of pH calculated for 8 May 2014 at 8:45–11:15 am, at 1–2 m above the seafloor (panels a–d). (d) The map was generated from measured data ('+' symbols) using ordinary kriging as implemented in the EasyKrig Matlab software (version 3.0, Dezhang Chu and Woods Hole Oceanographic Institution, downloaded from: ftp://globec.whoi.edu/pub/software/kriging/easy_krig/V3.0.2-Matlab2016b/ on 28 January 2019); based on the variogram, the following parameters were used: model: general exponential-Bessel, nugget: 0, sill: 1, length: 0.15, power: 2, hole scl: 0, range: 0.95. The spatial extent covered by panel d is indicated on panels a–c by a black rectangle.

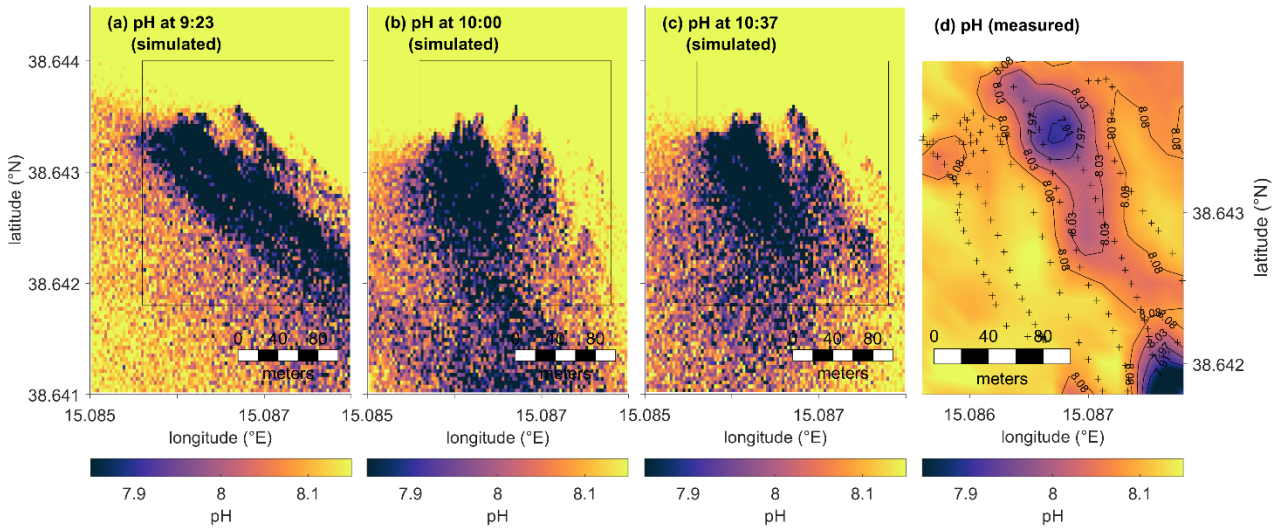

Figure S-15. (a–c) Simulated pH maps at three time points on 8 May 2014 for a total volume flow rate of 0.73 kg s^{-1} over the whole area (three times the best estimate presented in Figure 3), and (d) observed map of pH calculated for 8 May 2014 at 8:45–11:15 am, at 1–2 m above the seafloor (panels a–d). (d) The map was generated from measured data ('+' symbols) using ordinary kriging as implemented in the EasyKrig Matlab software (version 3.0, Dezhang Chu and Woods Hole Oceanographic Institution, downloaded from: ftp://globec.whoi.edu/pub/software/kriging/easy_krig/V3.0.2-Matlab2016b/ on January 28, 2019); based on the variogram, the following parameters were used: model: general exponential-Bessel, nugget: 0, sill: 1, length: 0.15, power: 2, hole scl: 0, range: 0.95. The spatial extent covered by panel d is indicated on panels a–c by a black rectangle.

S-14 Predicted excess DIC, pCO_2, and pH maps at 5–6 m above the seafloor

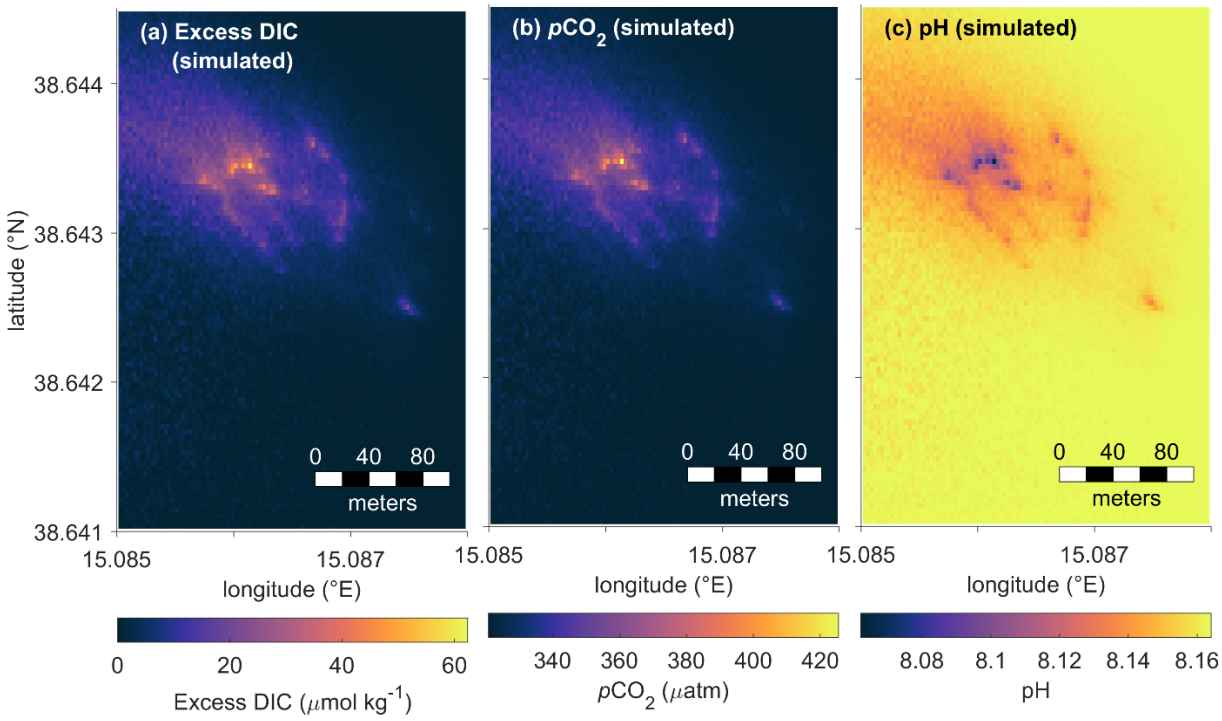

Figure S-16. (a) Simulated average excess DIC map, (b) simulated average pCO_2 map, (c) simulated average pH map. Values were calculated for a period exhibiting only limited variation in water current direction based on ADCP data (8 May 2014 at 8:45–11:15 am). Values were calculated at 5–6 m above the seafloor for a flow rate of 0.22 kg s^{-1} over the whole area. Note the different color axes compared to figures 3, S-14, and S-15.

S-15 References

(1) Gros, J.; Reddy, C. M.; Nelson, R. K.; Socolofsky, S. A.; Arey, J. S. Simulating gas–liquid–water partitioning and fluid properties of petroleum under pressure: Implications for deep-sea blowouts. *Environmental Science & Technology* **2016**, *50*, 7397–7408.

(2) Gros, J.; Socolofsky, S. A.; Dissanayake, A. L.; Jun, I.; Zhao, L.; Boufadel, M. C.; Reddy, C. M.; Arey, J. S. Petroleum dynamics in the sea and influence of subsea dispersant injection during *Deepwater Horizon*. *PNAS* **2017**, 201612518.

(3) Gros, J.; Dissanayake, A. L.; Daniels, M. M.; Barker, C. H.; Lehr, W.; Socolofsky, S. A. Oil spill modeling in deep waters: Estimation of pseudo-component properties for cubic equations of state from distillation data. *Marine Pollution Bulletin* **2018**, *137*, 627–637.

(4) Dissanayake, A. L.; Gros, J.; Socolofsky, S. A. Integral models for bubble, droplet, and multiphase plume dynamics in stratification and crossflow. *Environ Fluid Mech* **2018**, 1–36.

(5) Leonte, M.; Wang, B.; Socolofsky, S. A.; Mau, S.; Breier, J. A.; Kessler, J. D. Using carbon isotope fractionation to constrain the extent of methane dissolution into the water column surrounding a

natural hydrocarbon gas seep in the northern Gulf of Mexico. *Geochemistry, Geophysics, Geosystems* **2018**, *19*, 4459–4475.
(6) Jun, I. A numerical model for hydrocarbon bubbles from natural seeps within hydrate stability zone. Ph.D. Dissertation, Texas A&M University: College Station, Texas, 2018.
(7) Clift, R.; Grace, J. R.; Weber, M. E. *Bubbles, Drops, and Particles*; Academic Press: New York, 1978.
(8) King, M. B. *Phase Equilibrium in Mixtures*; Danckwerts, P. V., Ed.; International series of monographs in chemical engineering; Pergamon press: Oxford, 1969.
(9) Schwarzenbach, R. P.; Gschwend, P. M.; Imboden, D. M. *Environmental Organic Chemistry*; 2nd ed.; John Wiley & Sons, Inc.: Hoboken, 2003.
(10) Dhima, A.; de Hemptinne, J.-C.; Jose, J. Solubility of hydrocarbons and CO_2 mixtures in water under high pressure. *Ind. Eng. Chem. Res.* **1999**, *38*, 3144–3161.
(11) National Academies of Sciences, Engineering, and Medicine *The Use of Dispersants in Marine Oil Spill Response*; The National Academies Press: Washington, DC, 2019.
(12) Gros, J. Investigating the fate of petroleum fluids released in the marine environment with comprehensive two-dimensional gas chromatography and transport models. Ph.D. Dissertation, EPFL: Lausanne, 2016.
(13) Millero, F. J. The thermodynamics and kinetics of the hydrogen sulfide system in natural waters. *Marine Chemistry* **1986**, *18*, 121–147.
(14) Akinfiev, N. N.; Diamond, L. W. Thermodynamic description of aqueous nonelectrolytes at infinite dilution over a wide range of state parameters. *Geochimica et Cosmochimica Acta* **2003**, *67*, 613–629.
(15) Hayduk, W.; Laudie, H. Prediction of diffusion coefficients for nonelectrolytes in dilute aqueous solutions. *AIChE J.* **1974**, *20*, 611–615.
(16) Ferrell, R. T.; Himmelblau, D. M. Diffusion coefficients of nitrogen and oxygen in water. *J. Chem. Eng. Data* **1967**, *12*, 111–115.
(17) Zeebe, R. E. On the molecular diffusion coefficients of dissolved CO_2, HCO_3^-, and CO_3^{2-} and their dependence on isotopic mass. *Geochimica et Cosmochimica Acta* **2011**, *75*, 2483–2498.
(18) Duan, Z.; Sun, R.; Zhu, C.; Chou, I.-M. An improved model for the calculation of CO_2 solubility in aqueous solutions containing Na^+, K^+, Ca^{2+}, Mg^{2+}, Cl^-, and SO_4^{2-}. *Marine Chemistry* **2006**, *98*, 131–139.
(19) Fan, L.-S.; Yang, G. Q.; Lee, D. J.; Tsuchiya, K.; Luo, X. Some aspects of high-pressure phenomena of bubbles in liquids and liquid–solid suspensions. *Chemical Engineering Science* **1999**, *54*, 4681–4709.
(20) Fan, L.-S.; Tsuchiya, K. *Bubble Wake Dynamics in Liquids and Liquid–Solid Suspensions*; Elsevier, 1990.
(21) Beaubien, S. E.; De Vittor, C.; McGinnis, D. F.; Bigi, S.; Comici, C.; Ingrosso, G.; Lombardi, S.; Ruggiero, L. Preliminary Experiments and Modelling of the Fate of CO_2 Bubbles in the Water Column Near Panarea Island (Italy). *Energy Procedia* **2014**, *59*, 397–403.
(22) Rehder, G.; Leifer, I.; Brewer, P. G.; Friederich, G.; Peltzer, E. T. Controls on methane bubble dissolution inside and outside the hydrate stability field from open ocean field experiments and numerical modeling. *Marine Chemistry* **2009**, *114*, 19–30.
(23) Vielstädte, L.; Linke, P.; Schmidt, M.; Sommer, S.; Haeckel, M.; Braack, M.; Wallmann, K. Footprint and detectability of a well leaking CO_2 in the Central North Sea: Implications from a field experiment and numerical modelling. *International Journal of Greenhouse Gas Control* **2019**, *84*, 190–203.
(24) Goldman, J. C.; Dennett, M. R.; Frew, N. M. Surfactant effects on air-sea gas exchange under turbulent conditions. *Deep Sea Research Part A. Oceanographic Research Papers* **1988**, *35*, 1953–1970.

(25) Olsen, J. E.; Dunnebier, D.; Davies, E.; Skjetne, P.; Morud, J. Mass transfer between bubbles and seawater. *Chemical Engineering Science* **2017**, *161*, 308–315.
(26) Johansen, C.; Todd, A. C.; MacDonald, I. R. Time series video analysis of bubble release processes at natural hydrocarbon seeps in the Northern Gulf of Mexico. *Marine and Petroleum Geology* **2017**, *82*, 21–34.
(27) Rehder, G.; Brewer, P. W.; Peltzer, E. T.; Friederich, G. Enhanced lifetime of methane bubble streams within the deep ocean. *Geophysical Research Letters* **2002**, *29*, 21-1-21–4.
(28) Vielstädte, L.; Karstens, J.; Haeckel, M.; Schmidt, M.; Linke, P.; Reimann, S.; Liebetrau, V.; McGinnis, D. F.; Wallmann, K. Quantification of methane emissions at abandoned gas wells in the Central North Sea. *Marine and Petroleum Geology* **2015**, *68*, 848–860.
(29) Wang, B.; Socolofsky, S. A. A deep-sea, high-speed, stereoscopic imaging system for in situ measurement of natural seep bubble and droplet characteristics. *Deep Sea Research Part I* **2015**, *104*, 134–148.
(30) Römer, M.; Sahling, H.; Pape, T.; Bohrmann, G.; Spieß, V. Quantification of gas bubble emissions from submarine hydrocarbon seeps at the Makran continental margin (offshore Pakistan). *Journal of Geophysical Research: Oceans* **2012**, *117*.
(31) Riedel, M.; Scherwath, M.; Römer, M.; Veloso, M.; Heesemann, M.; Spence, G. D. Distributed natural gas venting offshore along the Cascadia margin. *Nature Communications* **2018**, *9*, 3264.
(32) Leifer, I. Characteristics and scaling of bubble plumes from marine hydrocarbon seepage in the Coal Oil Point seep field. *Journal of Geophysical Research: Oceans* **2010**, *115*, 1–20.
(33) Leifer, I.; Patro, R. K.; Bowyer, P. A Study on the Temperature Variation of Rise Velocity for Large Clean Bubbles. *J. Atmos. Oceanic Technol.* **2000**, *17*, 1392–1402.
(34) Schulze, G.; Schlünder, E. U. Physical absorption of single gas bubbles in degassed and preloaded water. *Chemical Engineering and Processing: Process Intensification* **1985**, *19*, 27–37.
(35) Alendal, G.; Drange, H. Two-phase, near-field modeling of purposefully released CO_2 in the ocean. *Journal of Geophysical Research: Oceans* **2001**, *106*, 1085–1096.
(36) Crounse, B. C. Modeling buoyant droplet plumes in a stratified environment. Thesis, Massachusetts Institute of Technology, 2000.
(37) Dissanayake, A. L.; DeGraff, J. A.; Yapa, P. D.; Nakata, K.; Ishihara, Y.; Yabe, I. Modeling the impact of CO_2 releases in Kagoshima Bay, Japan. *Journal of Hydro-environment Research* **2012**, *6*, 195–208.
(38) McGinnis, D. F.; Schmidt, M.; DelSontro, T.; Themann, S.; Rovelli, L.; Reitz, A.; Linke, P. Discovery of a natural CO_2 seep in the German North Sea: Implications for shallow dissolved gas and seep detection. *Journal of Geophysical Research* **2011**, *116*.
(39) Socolofsky, S. A.; Bhaumik, T. Dissolution of Direct Ocean Carbon Sequestration Plumes Using an Integral Model Approach. *Journal of Hydraulic Engineering* **2008**, *134*, 1570–1578.
(40) Zeebe, R.; Wolf-Gladrow, D. *CO_2 in Seawater: Equilibrium, Kinetics, Isotopes*; 2001.
(41) Somasundaran, P. *Encyclopedia of Surface and Colloid Science, Second Edition - Eight-Volume Set (Print)*; CRC Press, 2006.
(42) Pilson, M. E. Q. *An Introduction to the Chemistry of the Sea*; 2nd ed.; Cambridge University Press: Cambridge, 2013.
(43) United Nations Educational, Scientific and Cultural Organization (UNESCO) *Background papers and supporting data on the International Equation of State of Seawater, 1980 : Unesco/ICES/SCOR/IAPSO Joint Panel on Oceanographic Tables and Standards*; UNESCO technical papers in marine science; UNESCO: Geneva, 1981.
(44) Millero, F. History of the equation of state of seawater. *Oceanog.* **2010**, *23*, 18–33.
(45) Schmidt, M.; Linke, P.; Sommer, S.; Esser, D.; Cherednichenko, S. Natural CO_2 seeps offshore Panarea: A test site for subsea CO_2 leak detection technology. *Marine Technology Society Journal* **2015**, *49*, 19–30.

(46) Caliro, S.; Caracausi, A.; Chiodini, G.; Ditta, M.; Italiano, F.; Longo, M.; Minopoli, C.; Nuccio, P. M.; Paonita, A.; Rizzo, A. Evidence of a recent input of magmatic gases into the quiescent volcanic edifice of Panarea, Aeolian Islands, Italy. *Geophysical Research Letters* **2004**, *31*.

(47) Esposito, A.; Giordano, G.; Anzidei, M. The 2002–2003 submarine gas eruption at Panarea volcano (Aeolian Islands, Italy): Volcanology of the seafloor and implications for the hazard scenario. *Marine Geology* **2006**, *227*, 119–134.

(48) Dissanayake, A. L.; Jun, I.; Socolofsky, S. A. Numerical models to simulate oil and gas blowout plumes and associated chemical and physical processes of hydrocarbons. In *E-Proceedings of the 36th IAHR World Congress*; The Hague, 2015.

(49) Socolofsky, S. A.; Dissanayake, A. L.; Jun, I.; Gros, J.; Arey, J. S.; Reddy, C. M. Texas A&M Oilspill Calculator (TAMOC) modeling suite for subsea spills. In *Proceedings of the Thirty-Eighth AMOP Technical Seminar*; Environment Canada: Ottawa, 2015; pp. 153–168.

(50) Orr, J. C.; Epitalon, J.-M.; Gattuso, J.-P. Comparison of ten packages that compute ocean carbonate chemistry. *Biogeosciences Discussions* **2015**, *12*, 1483–1510.

(51) van Sebille, E.; Griffies, S. M.; Abernathey, R.; Adams, T. P.; Berloff, P.; Biastoch, A.; Blanke, B.; Chassignet, E. P.; Cheng, Y.; Cotter, C. J.; Deleersnijder, E.; Döös, K.; Drake, H. F.; Drijfhout, S.; Gary, S. F.; Heemink, A. W.; Kjellsson, J.; Koszalka, I. M.; Lange, M.; Lique, C.; MacGilchrist, G. A.; Marsh, R.; Mayorga Adame, C. G.; McAdam, R.; Nencioli, F.; Paris, C. B.; Piggott, M. D.; Polton, J. A.; Rühs, S.; Shah, S. H. A. M.; Thomas, M. D.; Wang, J.; Wolfram, P. J.; Zanna, L.; Zika, J. D. Lagrangian ocean analysis: Fundamentals and practices. *Ocean Modelling* **2018**, *121*, 49–75.

(52) Socolofsky, S. A.; Jirka, G. H. *Special Topics in Mixing and Transport Processes in the Environment*; 5th ed.; Texas A&M University: College Station, Texas, 2005.

(53) Jordt, A.; Zelenka, C.; von Deimling, J. S.; Koch, R.; Köser, K. The Bubble Box: Towards an Automated Visual Sensor for 3D Analysis and Characterization of Marine Gas Release Sites. *Sensors* **2015**, *15*, 30716–30735.

(54) Carpenter, J.; Bithell, J. Bootstrap confidence intervals: when, which, what? A practical guide for medical statisticians. *Statistics in Medicine* **2000**, *19*, 1141–1164.

(55) Millero, F. J. The marine inorganic carbon cycle. *Chem. Rev.* **2007**, *107*, 308–341.

(56) *Guide to best practices for ocean CO_2 measurements*; PICES Special Publication 3; North Pacific Marine Science Organization: Sydney, Canada, 2007; p. 191.

(57) Orr, J. C.; Epitalon, J.-M. Improved routines to model the ocean carbonate system: mocsy 2.0. *Geoscientific Model Development* **2015**, *8*, 485–499.

(58) Lewis, E.; Wallace, D. *Program developed for CO_2 system calculations*; 4735; Department of Applied Science Brookhaven National Laboratory, Carbon Dioxide Information Analysis Center, Oak Ridge National Laboratory: Oak Ridge, Tennessee, 1998.

(59) Dickson, A. G.; Goyet, C. *Handbook of methods for the analysis of the various parameters of the carbon dioxide system in sea water. Version 2*; ORNL/CDIAC--74, 10107773; 1994.

(60) Weiss, R. F. Carbon dioxide in water and seawater: the solubility of a non-ideal gas. *Marine Chemistry* **1974**, *2*, 203–215.

(61) Millero, F. J. Thermodynamics of the carbon dioxide system in the oceans. *Geochimica et Cosmochimica Acta* **1995**, *59*, 661–677.

(62) Mehrbach, C.; Culberson, C. H.; Hawley, J. E.; Pytkowicx, R. M. Measurement of the apparent dissociation constants of carbonic acid in seawater at atmospheric pressure. *Limnology and Oceanography* **1973**, *18*, 897–907.

(63) Lueker, T. J.; Dickson, A. G.; Keeling, C. D. Ocean pCO_2 calculated from dissolved inorganic carbon, alkalinity, and equations for K1 and K2: Validation based on laboratory measurements of CO_2 in gas and seawater at equilibrium. *Marine Chemistry* **2000**, *70*, 105–119.